

# Modeling Type-4 Wind in Weak Grids

Lingling Fan, *Senior Member, IEEE*

**Abstract**—An existing wind power plant at ERCOT experienced poorly damped and undamped low frequency oscillations at 3 ~ 4 Hz under weak grid condition. The objective of this paper is to shed the insight of the oscillation mechanism through linear system analysis. Two simplified models are developed and compared against a detailed model for Type-4 wind with weak grid interconnection. The detailed model includes grid-side converter’s outer power/voltage control, inner current controls, phase-locked loop (PLL), and transmission line electromagnetic dynamics. The first simplified model uses a first-order delay to replace the current control loop and ignores the transmission line dynamics and PLL. The second simplified model uses the same assumptions except that PLL is considered. Linearized system block diagrams for the two simplified models are derived and compared. The mechanism of the low-frequency oscillations are explained using eigenvalue analysis and the Root Locus method. The root causes are identified as weak grid, high wind power export, low voltage, and low PLL bandwidth. Further, the simplified model considering PLL dynamics is more accurate in low-frequency oscillation mode identification and system stability prediction.

**Index Terms**—Wind power plants, low-frequency oscillations, weak grids, phase-locked loop (PLL), linear system analysis

## I. INTRODUCTION

AN ERCOT wind power plant experienced poorly damped and undamped low-frequency oscillations under weak grid conditions [1]. The oscillation is at 3 ~ 4 Hz. The oscillations are undamped at high power output and poorly damped at lower power output. The objective of this paper is to present analytical models that are suitable for modeling and analysis for Type-4 wind with weak grid interconnections. The simplified models are expected to detect the low-frequency oscillations adequately and at the same time shed insights of the oscillation mechanism.

### A. Related Works

Weak grid interconnection of wind energy systems or voltage source converters (VSCs) pose stability issues. In addition, low grid voltage poses stability issues for VSC grid integration. Such phenomena have been mentioned in the following research [2]–[10].

Among the above references, References [2]–[4], [7] examined wind energy system weak grid interconnection stability issues. References [5], [9] examined stability issues of a VSC with weak grid interconnection. References [6], [8], [11] examined stability issues of different types of wind turbines at low voltage grid fault scenarios.

Low-frequency oscillations cannot be adequately modeled in a weak grid interconnection should the outer control loops

and/or PLL not be modeled. For example, in [7], 100 ~ 200 Hz oscillations are observed in a grid-connected Type-4 wind farm’s VSC with only current control modeled. Such oscillations can be mitigated through controller tuning as demonstrated in [7].

Low-frequency oscillations have been demonstrated in [2]–[6], [8]–[10]. The aforementioned references all have PLL and converters’ outer loops modeled. According to [2], ac voltage control and ac grid strength are two influencing factors of dynamic stability. A 2 MW permanent-magnet synchronous wind generator was studied in [2] and it has shown that with the system strength (indicated by short circuit ratio (SCR)) decreasing, the system will suffer oscillatory stability issues at approximately 10 Hz, which are demonstrated as one pair of the closed-loop system poles or eigenvalues moving to the right-half plane (RHP). A research paper published by Vestas engineers in 2013 [3] indicates that to facilitate weak interconnection, a wind farm is preferred to behave as a stiff voltage source to have better steady-state performance. This requires a fast voltage controller. However, fast voltage controller may result in resonances. Detailed stability analysis was not presented in [3].

In [4], low-frequency oscillations in the dc-link voltage in Type-3 wind with weak grid interconnections have been researched. A reduced-order model is proposed for stability analysis with wind being treated as current sources. High-frequency dynamics related to induction machines and transmission lines are ignored. Similar analysis has been conducted to demonstrate 10 Hz oscillations due to a VSC with weak grid condition [9], 6 Hz oscillations in Type-4 wind due to grid voltage sag [6], and 9 Hz oscillations in Type-3 wind due to grid voltage sag [8]. The four reference papers indicate both PLL and converter’s voltage controller play roles in low-frequency oscillations. Investigation of the impact of PLL on stability can also be found in [5], [10]–[12].

### B. Contributions

Detailed models provide accurate analysis results. A detailed model for Type-4 wind farm with machine dynamics, generator-side converter controls, grid-side converter controls, PLL and grid dynamics is presented in [2]. Analysis of a grid-connected VSC in [5] is also based on detailed model with grid dynamics, PLL and converter controls represented.

While the benefit of detailed models is obvious, to provide insights of oscillation mechanism, simplified models are sought. Practice in Vestas [3] indicates that for power grid dynamics, the wind machine dynamics and generator-side converter controls can be omitted. The omission of wind machine dynamics is also adopted in [4] for modeling Type-3 wind farm to study low-frequency oscillations in dc-link voltages. In [4],

a Type-3 wind farm is treated as two current sources from the rotor-side converter and the grid-side converter. The current orders are determined by the outer power and voltage controls. Current control loops are ignored while PLL is considered in the study model.

Further simplified model with PLL ignored has been investigated in the author's prior work [13]. Using this model, we successfully explained the causes of low-frequency oscillations due to low SCR.

Though there have been plenty of research available on modeling low-frequency oscillations in a Type-4 wind or a VSC with weak grid interconnection, it is still not clear up to which stage of simplification, a model can still provide adequate analysis of low-frequency oscillations and what is the impact of ignoring or not ignoring PLL on accurate oscillation analysis. Further, there is a need of a summary paper on different types of models as well as their comparison. This paper addresses the above two concerns.

Generally, dynamic model reduction can be classified into two categories. The first approach is based on physical system understanding and manual reduction, e.g., [14]. In [14], the reduced model is derived by ignoring transmission line dynamics and current control dynamics. The second approach is based on system reduction theory, e.g., singular perturbation method used in [15]. Implementation of singular perturbation method also requires physical system understanding to separate fast and slow dynamics. The first approach is adopted in this paper to obtain simplified models through trial and error. Since the focus of this paper is to shed insights on low-frequency oscillations through model simplifications, using formalized method for model reduction will be the topic of further research.

In this paper, we present two types of nonlinear simplified models and derive the related linear system block diagrams. Through the Root-Locus method and using the block diagrams, oscillation mechanisms as well as influencing factors are identified.

A detailed model with converter's current feedback controls, outer control loops, PLL and grid dynamics is built as the benchmark model. The two simplified models are compared against the detailed model for eigenvalue plots and simulation results. The comparison against the benchmark model indicates which model is better in capturing essential dynamics related to wind with weak grid interconnection.

In addition to the modeling and validation efforts, a highlight of the contribution is the explanation of the low-frequency oscillation mechanism using linear system block diagrams. This approach clearly explains the effect of PLL bandwidth on system stability.

### C. Organization

The rest of the paper is organized as follows. Section II presents the benchmark model. Section III presents the two simplified model with inner current control loop being replaced by a first-order delay, and grid dynamics ignored. The two simplified models differ from the inclusion or omission of PLL dynamics. Section IV presents the comparison of the two

models against the benchmark model on small-signal analysis and time-domain simulation. Section V presents the symbol-based linear systems using simplified models. Investigation of low-frequency oscillation mechanism is then conducted using eigenvalue analysis and the Root-Locus method. Section VI concludes the paper.

## II. THE DETAILED MODEL (MODEL 1)

The study system is shown in Fig. 1 and the modeling block diagram of the system is shown in Fig. 2.

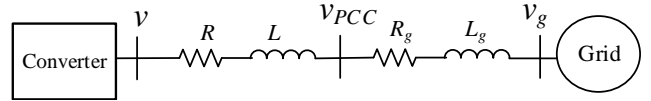


Fig. 1. Circuit diagram of the system.

A Type-4 wind farm model consists of grid-side converter controls (outer power and voltage control, inner current control), PLL, dc-link dynamics, machine-side converter controls and permanent magnetic synchronous machine dynamics.

For power system dynamic study that are concerned with dynamics in the bandwidth of 0 ~ 10 Hz, the dc-link dynamics, machine-side converter controls and machine dynamics are ignored. The similar assumption was also made in Type-3 wind farm stability analysis in [4].

### A. Reference frames

PLL includes  $dq$  to  $abc$  reference frame conversion. A critical step of developing analytical models suitable for small-signal analysis is to replace the  $abc$ -frame by the grid  $dq$ -frame, since variables in the  $abc$  frame are periodic at steady-state. With such variables, linearization at an operating condition with state variables being constant is not possible.

The circuit dynamics are also modeled in the grid  $dq$ -frame. The grid  $dq$ -frame has its  $d$ -axis aligned with the grid voltage's space vector  $\vec{v}_g$ . The grid is assumed to have a constant nominal frequency  $\omega_0$  and the grid voltage's initial angle is 0. Therefore, the space vector of the grid voltage can be expressed as:  $\vec{v}_g = V_g e^{j\omega_0 t}$ , where  $V_g$  is the magnitude.

The current controllers deal with  $dq$  currents based on the converter  $dq$ -reference frame. This  $dq$ -frame aligns its  $d$ -axis with the PCC voltage space vector  $\vec{v}_{PCC}$ .

The three-phase currents  $i_a$ ,  $i_b$  and  $i_c$  form a space vector

$$\vec{i} = \frac{2}{3} \left( i_a + i_b e^{j\frac{2\pi}{3}} + i_c e^{-j\frac{2\pi}{3}} \right).$$

The PLL outputs an angle  $\theta$  to track the angle of PCC voltage's space vector (notated as  $\theta_{PCC}$ ). The converter  $dq$ -frame currents, the grid  $dq$ -frame currents, and the current space vector have the following relationship:

$$(i_d^c + j i_q^c) e^{j\theta} = \vec{i} = (i_d^g + j i_q^g) e^{j\omega_0 t},$$

where the superscript  $c$  notates the converter  $dq$ -frame and the superscript  $g$  notates the grid  $dq$ -frame.

Therefore, the currents in the two  $dq$ -frames have the following relationship:

$$(i_d^c + j i_q^c) e^{j\Delta\theta} = i_d^g + j i_q^g,$$

where  $\Delta\theta = \theta - \omega_0 t$ .

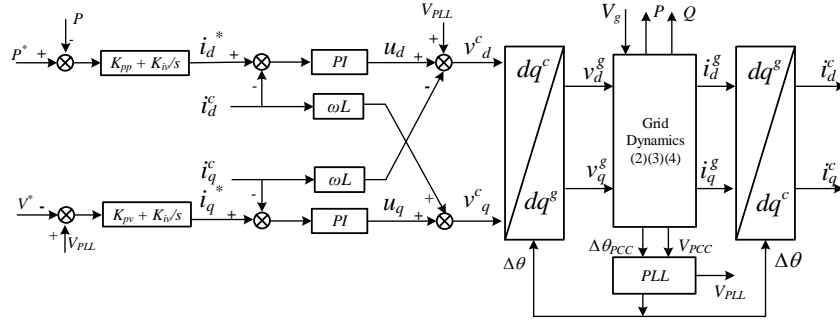


Fig. 2. Block diagram of the system.

### B. PLL

A second-order PLL (details can be referred in Chapter 6 [16]) is modeled and shown in Fig. 3. After the  $abc/dq$  block with  $\theta$  as the input angle, the PCC voltage is in the converter  $dq$ -frame.

$$V_{PCC}e^{j(\theta_{PCC}-\theta)} = V_{PCC}e^{j(\Delta\theta_{PCC}-\Delta\theta)} = (v_{PCC,d}^c + jv_{PCC,q}^c),$$

where  $\Delta\theta_{PCC} = \theta_{PCC} - \omega_0 t$  and  $V_{PCC}$  is the magnitude of the PCC voltage.

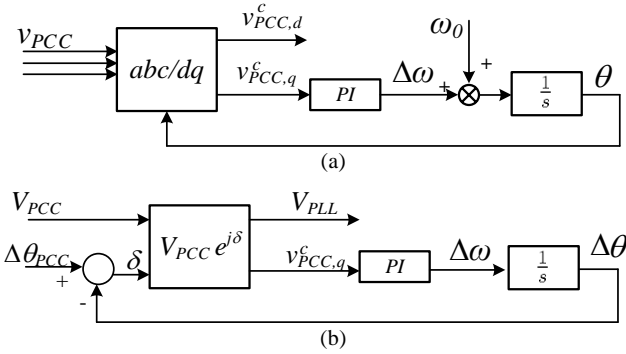


Fig. 3. Block diagrams of a PLL. (a) Original PLL. (b) PLL in  $dq$ -frames.

The  $dq$  components are:

$$\begin{aligned} V_{PLL} &= v_{PCC,d}^c = V_{PCC} \cos(\Delta\theta_{PCC} - \Delta\theta) \\ v_{PCC,q}^c &= V_{PCC} \sin(\Delta\theta_{PCC} - \Delta\theta) \end{aligned} \quad (1)$$

$v_{PCC,q}^c$  is fed into a PI control block to generate the frequency deviation  $\Delta\omega$ . Integrating the frequency deviation results in  $\Delta\theta$ . Since the input of a PI controller will be zero at steady-state, this control guarantees that  $v_{PCC,q}^c$  becomes 0 at steady-state. Or, the  $d$ -axis of the converter frame is aligned with the PCC voltage.

### C. Grid dynamics

The converter's output voltages  $v_d^c$  and  $v_q^c$  are first converted to  $v_d^g$  and  $v_q^g$ :

$$v_d^g + jv_q^g = (v_d^c + jv_q^c)e^{j\Delta\theta}.$$

Together with the grid voltage, they are treated as the input of the grid dynamics block and the outputs of this block include currents in the grid  $dq$ -frame ( $i_d^g, i_q^g$ ) and the PCC voltage

magnitude  $V_{PCC}$  and the angle  $\Delta\theta_{PCC}$ . The dynamics of the transmission line are described in (2).

$$\begin{aligned} \tilde{R}i_d^g + \tilde{L}\frac{di_d^g}{dt} - \omega_0\tilde{L}i_q^g &= v_d^g - V_g \\ \tilde{R}i_q^g + \tilde{L}\frac{di_q^g}{dt} + \omega_0\tilde{L}i_d^g &= v_q^g \end{aligned} \quad (2)$$

where  $V_g$  is the magnitude of the grid voltage,  $\tilde{R} = R + R_g$  and  $\tilde{L} = L + L_g$ . Further,  $v_{PCC,d}^g$  and  $v_{PCC,q}^g$  can be computed using  $i_d^g, i_q^g$  and their derivatives.

$$\begin{aligned} v_{PCC,d}^g &= R_g i_d^g + L_g \frac{di_d^g}{dt} - \omega_0 L_g i_q^g + V_g \\ v_{PCC,q}^g &= R_g i_q^g + L_g \frac{di_q^g}{dt} + \omega_0 L_g i_d^g \end{aligned} \quad (3)$$

$V_{PCC}$  and  $\Delta\theta_{PCC}$  can be obtained based on the  $dq$  components from (3). The real power and reactive power measured at the PCC voltage can be computed using  $V_{PCC}$  and the  $dq$ -axis currents based on the converter  $dq$  frame.

$$P = V_{PCC}i_d^c, \quad Q = -V_{PCC}i_q^c. \quad (4)$$

Eq. (4) illustrates the principle of vector control. It indicates that  $P$  and  $Q$  can be controlled separately. In order to adjust  $P$ , we only need to adjust the  $d$ -axis current  $i_d^c$ . Since  $P$  is proportionally related to the  $d$ -axis current, negative feedback control can be adopted. In order to adjust  $Q$  or voltage, we only need to adjust the  $q$ -axis current  $i_q^c$ . Moreover, the feedback control should be a positive feedback control since  $Q$  is proportional to  $-i_q^c$ .

The block diagram of the entire system is shown in Fig. 2. The outer power and voltage controls are also included.

### III. THE SIMPLIFIED MODELS (MODELS 2 & 3)

In the first simplified model (Model 2), we ignore electromagnetic dynamics in the transmission line network and treat the network as an algebraic model. Note that in the detailed model, the input of the network dynamics includes converter voltages and the output includes current and the PCC voltage. With the algebraic model representation, if the same input and output are used, algebraic loops will be present in the simulation model. This is due to the decoupling terms related to the currents and the feed forward term related to the voltage  $V_{PLL}$  used in the converter control (shown in Fig. 2). Thus it is necessary to treat the VSC as a current source instead of a voltage source. The  $dq$ -axis currents injected to the grid are assumed to have a delay from the current orders. A first-order

transfer function  $\frac{1}{1+\tau s}$  is used to represent the current tracking. Such approximation has been used in analytical tuning of the outer control loops of vector control of VSCs in grid interconnection [17] (Chapter 8) and in motor drives [18] (Chapter 12).

We aggregate the current feedback control dynamics and the effect of PLL into first-order systems in Model 2, with the current references as the inputs and the current measurements as the outputs.

Though 20 ms is a typical value of the delay, during weak grid conditions, the effect of phase-locked-loop (PLL) will make the delay value longer [19]. The entire vector control now has power error and voltage error as the inputs and its outputs are  $i_d^c$  and  $i_q^c$ .

Hereafter, the superscript *c* will be omitted.

The second simplified model (Model 3) is similar as Model 2 except that PLL dynamics is included. The block diagrams of the two models are presented in Fig. 4.

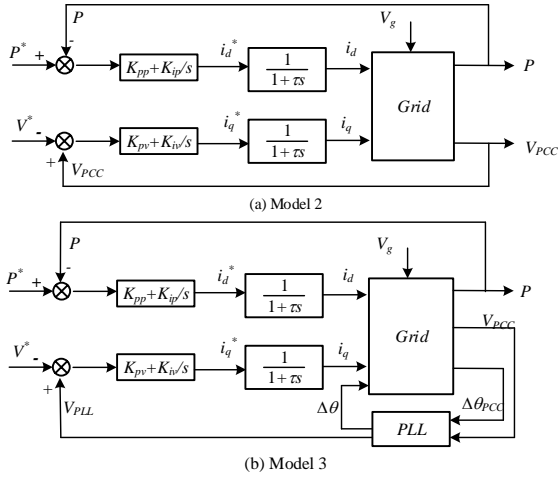


Fig. 4. Model 2 and Model 3.

The difference in Model 3 and Model 2 resides not only the inclusion of PLL dynamics, but also the selection of time constant  $\tau$ . In Model 2, the first-order transfer function of current tracking includes PLL effect.  $\tau$  will be adjusted when the system strength is varying. In Model 3, since PLL dynamics is explicitly included,  $\tau$  will keep intact.

#### A. Selection of Time Constant $\tau$ for Model 2

First, we will show how  $\tau$  should be selected in Model 2 related to different grid strength. The linear models from the current orders to the  $dq$  currents are obtained numerically from Model 1 using MATLAB function *linmod*.

PLL dynamics and grid dynamics are considered while the outer loops are not considered. The parameters of the system are given in Table I. The current loop is designed to have a 500 Hz bandwidth should the PCC voltage be stiff. The PLL bandwidth is designed to be 70 Hz. For steady-state condition, the power transfer level is 0.5 pu real power with unity power factor measured at  $v_g$ . A 0.1 pu step change is enforced at  $i_d^*$  at  $t = 0.05$  seconds. The responses of  $i_d$ ,  $i_q$ ,  $(\theta - \theta_{PCC})$ , and  $(V_{PLL} - V_{PCC})$  are shown in Fig. 5.

TABLE I  
PARAMETERS OF THE SYSTEM

$R$	0.001 pu	$X$	0.05 pu
$R_g$	$0.1X_g$	$X_g$	varying from 0.1 pu to 1 pu
$K_{pPLL}$	200 rad/(pu.s)	$K_{iPLL}$	$6 \times 10^4$ rad/(pu.s <sup>2</sup> )
$K_p$	0.4758 pu	$K_i$	3.2655 pu/s

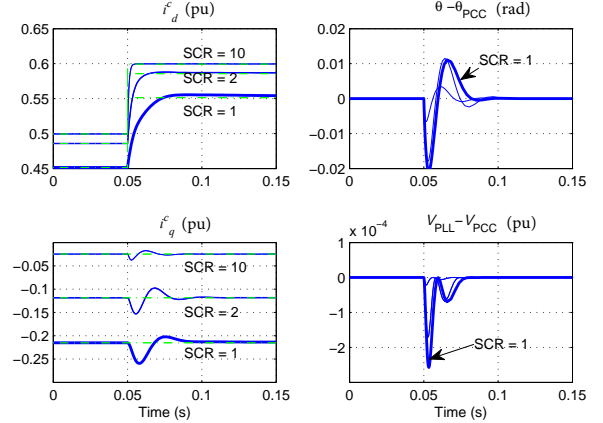


Fig. 5. Simulation results of step change in  $i_d^*$ .

Bode plots from  $i_d^*$  to  $i_d$  of the closed-loop system are shown in Fig. 6. From both the simulation plots and the Bode plots, it is clear to see that the response of the current tracking becomes slower when the grid becomes weaker.

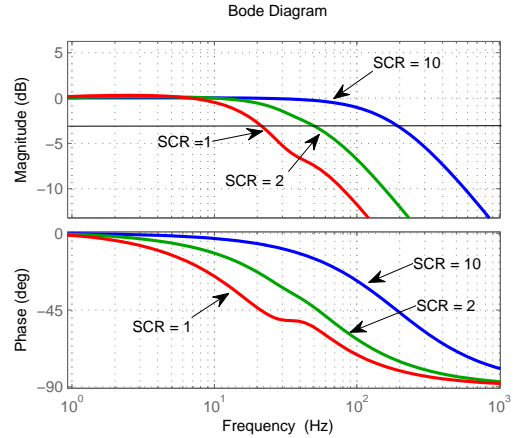


Fig. 6. Bode plots:  $i_d/i_d^*$ . The bandwidths are 20 Hz for SCR = 1, 50 Hz for SCR = 2, and 200 Hz for SCR = 10.

Remarks: From Fig. 6, the bandwidth of current order tracking reduces when the system strength reduces. When SCR is 10, the bandwidth is 200 Hz. Hence, the time constant for the first-order transfer function  $\tau$  can be chosen as 5 ms. When SCR is 2 or 1, the bandwidth becomes 50 Hz or 20 Hz, indicating the time constant to be 20 ms or 50 ms. Table II lists the time constant number versus the grid strength.

#### IV. COMPARISON OF MODELS

In this section, Model 2 and Model 3 are compared against Model 1. Both eigenvalue calculation and time-domain simulation are carried out. Our objective is to find out which simplified model can give more accurate eigenvalues and

TABLE II  
 $\tau$  VERSUS  $X_g$  AND SCR

$X_g$	SCR	$\tau$ (s)
0.1	10	0.005
0.2	5	0.01
0.5	2	0.02
0.75	1.33	0.035
0.85	1.177	0.0425
1.0	1	0.05

time-domain responses related to the low-frequency oscillation mode.

The parameters of the system are given in Table III. The SCR is 1.33. Three sets of PLL parameters will be used in this project and their bandwidths are computed using closed-loop PLL transfer function (also shown as  $G_{PLL}$  in Fig. 16).

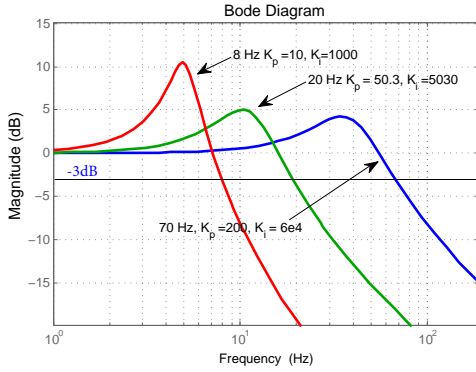


Fig. 7. Bode plots for three PLLs and their bandwidths.

To test the robustness of the simplified models, PLL with 20 Hz bandwidth is chosen for Model 3 in this Section.

TABLE III  
PARAMETERS OF THE SYSTEM AT BASE CASE

Converter RL filter	$R = 0.001$ pu, $X = 0.05$ pu
Grid RL parameter	$R_g = 0.01$ , $X_g = 0.75$ pu
PLL's parameters	$K_{pPLL} = 50.3$ , $K_{iPLL} = 5030$ (20 Hz) $K_{pPLL} = 200$ , $K_{iPLL} = 6 \times 10^4$ (70 Hz) $K_{pPLL} = 10$ , $K_{iPLL} = 1000$ (8 Hz)
Current control	$K_p + \frac{K_i}{s} = 0.4758 + \frac{3.2655}{s}$
Power control	$K_{pp} + \frac{K_{ip}}{s} = 0.4 + \frac{40}{s}$
Voltage control	$K_{pv} + \frac{K_{iv}}{s} = 0.25 + \frac{2.5}{s}$
Power level	1 pu
PCC voltage level	1 pu
$\tau$ in Model 2	0.035 s
$\tau$ in Model 3	0.017 s

### A. Comparison of Eigenvalues

Eigenvalue computation is carried out for the three models. With nonlinear dynamic models built in MATLAB/Simulink and initial values of all states calibrated and assigned, the dynamic models will all achieve flat runs when there is no dynamic event applied. Based on the same operating conditions, we use MATLAB's function *linmod* to find the linearized system's models described in the form of  $\Delta \dot{x} = A\Delta x + B\Delta u$  and  $\Delta y = C\Delta x + D\Delta u$ . The four matrices  $A$ ,  $B$ ,  $C$ , and  $D$  will be provided. Essentially, *linmod* uses a numerical method (small perturbation method) to find those matrices.

The power level at 0.8 pu, 1.0 pu, and 1.25 pu will be used for steady-state computation to initialize the state variables used in the three nonlinear models. Table IV lists the eigenvalues from the three models at the three operating conditions.

Model 1 includes two state variables related to the transmission line dynamics  $i_d$  and  $i_q$ , and two state variables related to the PLL, two state variables related to the power controller and the voltage controller, and two state variables related to the current controllers. Total, there are eight eigenvalues. Model 2 does not have the transmission line dynamics and PLL dynamics. There are four state variables: two related to the power controller and voltage controller and two related to two first-order delay blocks of the current tracking. The number of the eigenvalues is four. Model 3 has six eigenvalues, with two related to the power and voltage controllers, two related to the current blocks, and the two related to the PLL dynamics.

TABLE IV  
COMPARISON OF EIGENVALUES FROM THE DETAILED MODEL AND THE SIMPLIFIED MODEL

Model	$P = 0.8$	$P = 1$	$P = 1.25$
1	$-252.23 \pm j135.94$	$-249.17 \pm j152.48$	$-242.94 \pm j169.06$
	<b><math>-14.54 \pm j35.72</math></b>	<b><math>-4.34 \pm j27.87</math></b>	<b><math>9.77 \pm j15.12</math></b>
	$-42.83$	$-43.65 \pm j1.52$	$-56.09$
	$-29.77$		$-45.66$
	$-6.82 \pm j0.05$	$-6.83 \pm j0.06$	$-6.8490 \pm j0.07$
2	<b><math>-6.67 \pm j22.90</math></b>	<b><math>-0.72 \pm j22.43</math></b>	<b><math>15.13 \pm j13.35</math></b>
	$-27.81 \pm j17.71$	$-31.55 \pm j15.46$	$-38.78 \pm j7.10$
3	$-32.48 \pm j56.71$	$-37.69 \pm j55.36$	$-42.50 \pm j53.98$
	<b><math>-15.02 \pm j27.62</math></b>	<b><math>-3.55 \pm j26.33</math></b>	<b><math>11.62 \pm j14.40</math></b>
	$-48.86 \pm j10.79$	$-51.74 \pm j10.60$	$-54.66 \pm j9.82$

Table IV shows that a pair of complex conjugate eigenvalues are identified by all three models (in bold font). This mode is significantly influenced by the power exporting level. With an increasing power, the system can be unstable due to the pair of eigenvalues moving to the RHP. It can also be shown that the critical mode's eigenvalues in Model 3 are more accurate compared to those in Model 2.

Both Model 2 and Model 3 introduce non-existing modes due to simplification. This type of phenomena was also documented in the literature by other researchers, e.g., [20]. In [20], two models of VSC-HVDC are compared. One is the detailed model and the other is a simplified model based on DigSilent Power Factory. In this paper, Model 2 produces one non-existing mode while Model 3 produces two non-existing modes. Note that when power level increases, the fake modes in both models all move towards the left half plane (LHP). In addition, the modes all have very large damping ( $\geq 49.61\%$ ). Hence, those modes will not manifest as weak grid dynamic phenomena. That is, reducing grid strength or increasing wind power will not make those modes dominant.

The effect of power exporting is further explained using eigenvalue loci. Fig. 8 shows the loci for Model 1 while Fig. 9 shows the loci for Model 2 and 3. The eigenvalue loci of Model 2 and Model 3 are compared with those of Model 1 in one plot. Fig. 10 shows the comparison of Model 2 and Model 1, while Fig. 11 shows the comparison of Model 3 and Model 1. Similarly, the effect of  $X_g$  is shown in two figures: Figs. 12 and 13. It can be seen that for the critical low-frequency

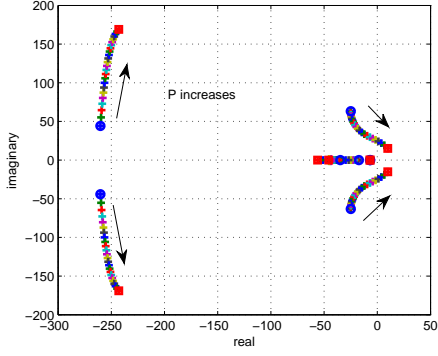


Fig. 8. Eigenvalue loci of a varying  $P$  for Model 1.

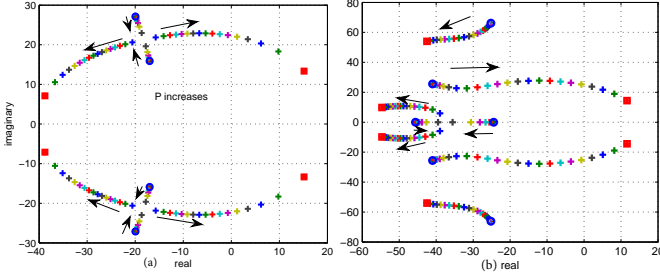


Fig. 9. Eigenvalue loci of a varying  $P$  for Model 2 (a) and Model 3 (b).

mode, Model 3 matches better to Model 1 compared to Model 2.

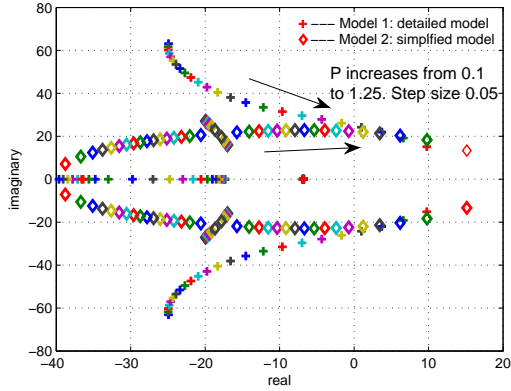


Fig. 10. Comparison of Model 2 and Model 1 on the effect of power export.  $X_g = 0.75$  pu.

Remarks: From the above comparison, it can be clearly shown that with PLL dynamics included, for the critical low-frequency oscillation mode, Model 3 matches better to Model 1 compared to Model 2.

### B. Comparison of Time-domain Simulation

Time-domain simulation comparison is also conducted for the three models. The small disturbance responses of the systems can be predicted accurately by eigenvalue analysis. In this subsection, a large disturbance (line tripping) is used to initiate dynamic responses.

Line tripping is reflected by a change of  $X_g$ . The original  $X_g$  is set to 0.6 pu with the assumption of two parallel transmission lines in place. At  $t = 1$  s, one of the lines is

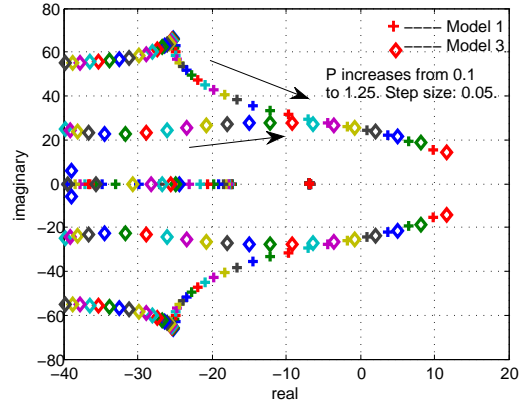


Fig. 11. Comparison of Model 3 and Model 1 on the effect of power export.  $X_g = 0.75$  pu.

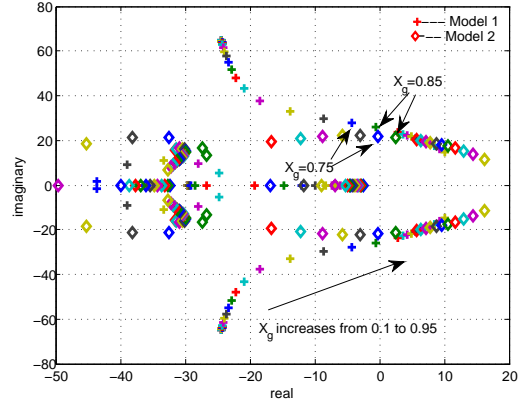


Fig. 12. Comparison of Models 2 and 1 on the effect of SCR.  $P = 1$  pu.

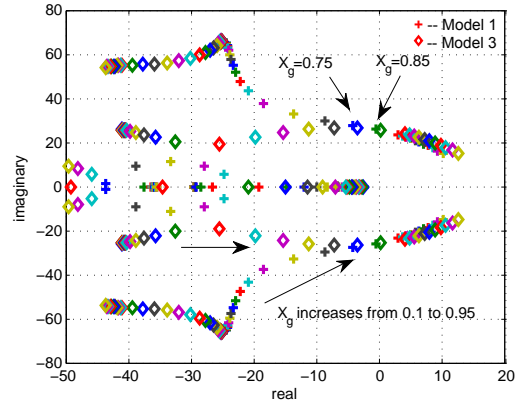


Fig. 13. Comparison of Models 3 and 1 on the effect of SCR.  $P = 1$  pu.

tripped. The resulting  $X_g$  is 0.75 pu. Simulation studies for all three models are conducted. For Model 2, the time constant  $\tau$  is adjusted to reflect the system strength change. Before 1 second,  $\tau$  is 0.03 s. After 1 second,  $\tau$  is 0.0375 s. For Model 3,  $\tau$  is 0.017 s and keeps intact. The simulation results are presented in Fig. 14.

The time-domain simulation results indicate again that Model 3 matches Model 1 much better.



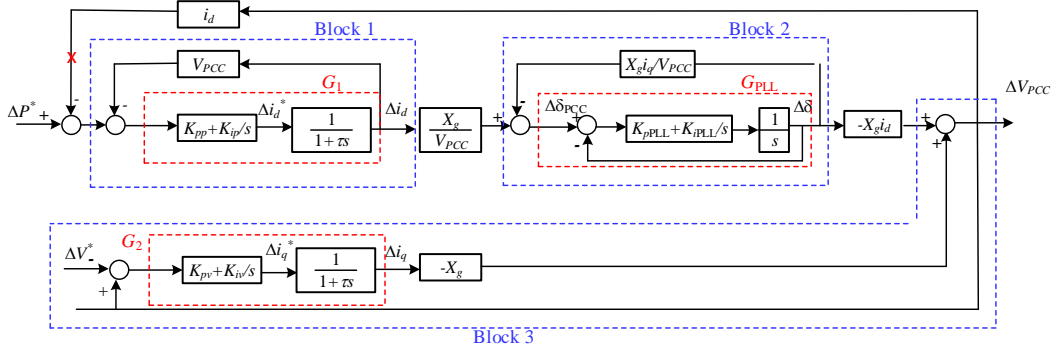


Fig. 16. Block diagrams of the linearized system (Model 3).

(18) is the same as (9). Thus Model 2 and Model 3 are equivalent if PLL dynamic is ignored. To better examine the effect of PLL dynamics, the block diagram in Fig. 16 will be aggregated to have six series connected blocks if the loop is broken at the point marked as **X**.

For Block 3, the feedforward gain from the input to the output is 1. The feedback loop gain is  $-X_g G_2$ . Considering the reference signal  $\Delta V^*$  as a disturbance and the feedback loop is a positive feedback, then the transfer function from the input to the output should be

$$G_{\text{Block3}} = \frac{\text{Feedforward gain}}{1 - \text{Loopgain}} = \frac{1}{1 + X_g G_2} \quad (19)$$

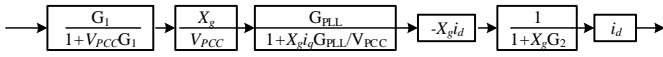


Fig. 17. The open-loop system of Model 3.

#### D. Mechanism of Low-Frequency Oscillations

Using the open-loop transfer function in Fig. 17, we are able to investigate the mechanism of low-frequency oscillations thoroughly.

The open-loop transfer function is as follows.

$$G_{OL} = -\frac{(X_g i_d)^2}{V_{PCC}} \underbrace{\frac{G_1}{1 + V_{PCC} G_1}}_{\text{Block 1}} \underbrace{\frac{G_{PLL}}{1 + \frac{X_g i_d}{V_{PCC}} G_{PLL}}}_{\text{Block 2}} \underbrace{\frac{1}{1 + X_g G_2}}_{\text{Block 3}} \quad (20)$$

where

$$G_1 = \left( K_{pp} + \frac{K_{ip}}{s} \right) \frac{1}{1 + \tau s}$$

$$G_2 = \left( K_{pv} + \frac{K_{iv}}{s} \right) \frac{1}{1 + \tau s}$$

$$G_{PLL} = \frac{K_{pPLL} s + K_{iPLL}}{s^2 + K_{pPLL} s + K_{iPLL}}$$

a) *Effect of PLL Parameters: Eigenvalue Analysis Versus Root-Locus Method:* The effect of PLL parameters is first investigated by examining the *eigenvalues* based on the linear system shown in Fig. 16 (with the loop closed) and the eigenvalues based on Model 1.

The impact of PLL's proportional gain on the system eigenvalues is shown in Fig. 18. The left column presents the results based on Model 1 while the right column presents the results based on Model 3. It can be seen that both the detailed model and the simplified model show that higher bandwidth of PLL makes the system more stable.

It can be seen that the simplified model gives comparable or more conservative estimation on the system oscillations. For example, when SCR is at 1.3 and the gain of PLL is reaching 100, Model 1 shows the pair of eigenvalues are at  $-10 \pm j16$  while Model 3 shows the pair of the eigenvalues are at  $-5 \pm j20$ .

A further comparison is conducted for SCR at 1. The PLL's proportional gain starts from 0.01. Here we set  $K_{iPLL} = 100 K_{pPLL}$  to follow the PLL parameter setting of the 20 Hz bandwidth presented in Table III.

It can be seen from Fig. 19 that for a wide range of PLL bandwidths, the simplified model and the detailed model show similar dynamic responses for the critical mode. Both systems show that when the proportional gain is less than 50, the system is unstable. Therefore, the proposed simplified model (Model 3) is suitable to capture the essential dynamics related to wind with weak grid interconnection and the impact of PLL.

Although Fig. 19 shows that when the gain becomes very small, reducing the gain may help system stability, we have to consider those scenarios are not realistic. In real-world applications, PLL bandwidth is usually in a certain range (10 Hz  $\sim$  100 Hz). For example, for FACTS applications [21], the proportional gain is 100 and the integrator's gain is 2000 based on per unit inputs. The bandwidth is approximately 16 Hz based on the closed-loop system Bode plot. In [22], the bandwidth of a PLL is 100 Hz and the parameters are  $K_p = 2.62$  and  $K_i = 1650$  based on 120 V voltage inputs. In the per unit scale, the two parameters are 445 and 28,000. In [19], the gains are  $K_p = 50.3$ ,  $K_i = 5030$  based on per unit inputs. The resulting PLL bandwidth is approximately 20 Hz.

In general, in the range of 10 Hz to 100 Hz PLL bandwidth, the system is more stable with higher PLL bandwidth. Time-domain simulation is carried out using Model 1 to examine the effect of PLLs. The dynamic responses are shown in Fig. 20. Note that the resistance of the grid  $R_g$  is no longer ignored in the validation process ( $R_g = 0.01$  pu). It can be seen that when the PLL bandwidth is 20 Hz, a 4 Hz oscillation becomes undamped and the system loses stability. On the other hand,

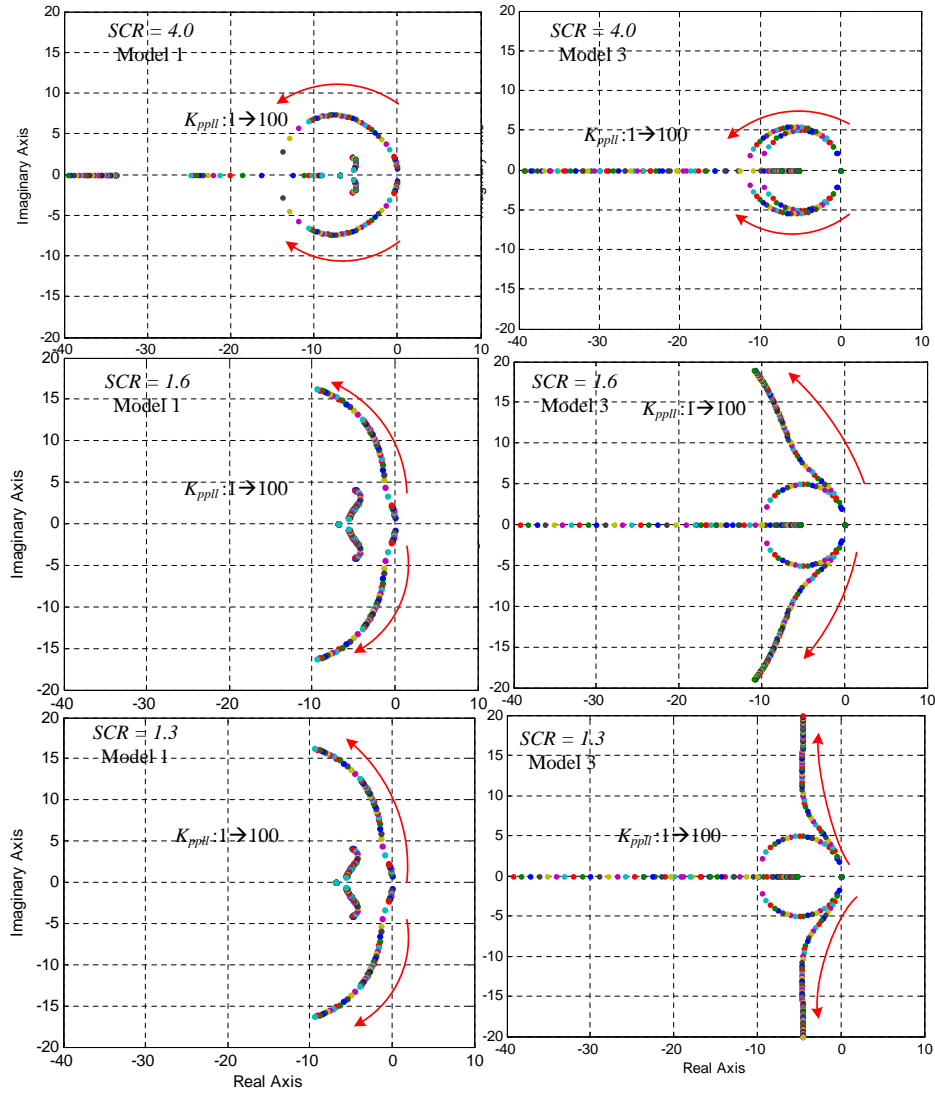


Fig. 18. Eigenvalue plots for a varying PLL proportional gain.  $K_{iPLL} = 5K_{pPLL}$ . Other controller parameters follow Table III. Power exporting level is at 1 pu. Left Column: Model 1; Right Column: Model 3.

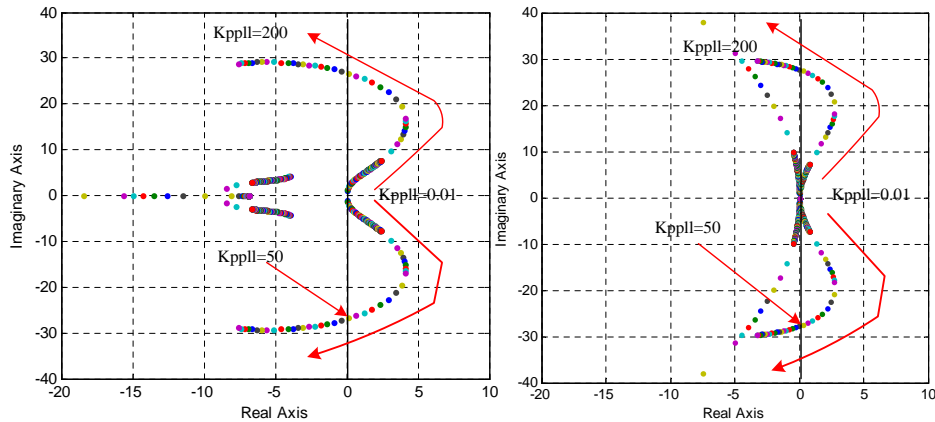


Fig. 19. Eigenvalue plots for a varying PLL proportional gain.  $K_{iPLL} = 100K_{pPLL}$ . SCR = 1, and power level is 0.8 pu. Left Column: Model 1; Right Column: Model 3.

when the PLL bandwidth is 70 Hz, the system is stable and there is no oscillation.

We next use *Root-locus Method* to conduct stability anal-

ysis. The root loci based on  $G_{OL}$  is shown in Fig. 21 (SCR = 1,  $P = 0.8$ ). Stability or instability of the closed-loop system can be identified by checking the gain required when the loci

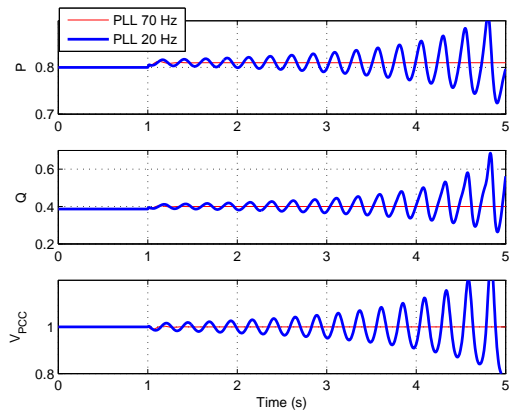


Fig. 20. Dynamic response of  $P$ ,  $Q$  and  $V_{PCC}$  of Model 1 subject to 0.01 pu power reference increase at 1 s.

pass the imaginary axis. When the loop is closed, the gain is 1. Hence, if the gain from the root loci is less than 1, then the closed-loop system is unstable. The zoom-in figure in Fig. 21 gives the gains. When PLL's bandwidth is 70 Hz, the gain is 1.27, which indicates the closed-loop system is stable. When PLL's bandwidth is 20 Hz or 8 Hz, the gains are less than 1, which indicates instability. For a transfer function without considering PLL or PLL's bandwidth is infinity and  $G_{PLL} = 1$ , the gain is 1.28 and the system is stable.

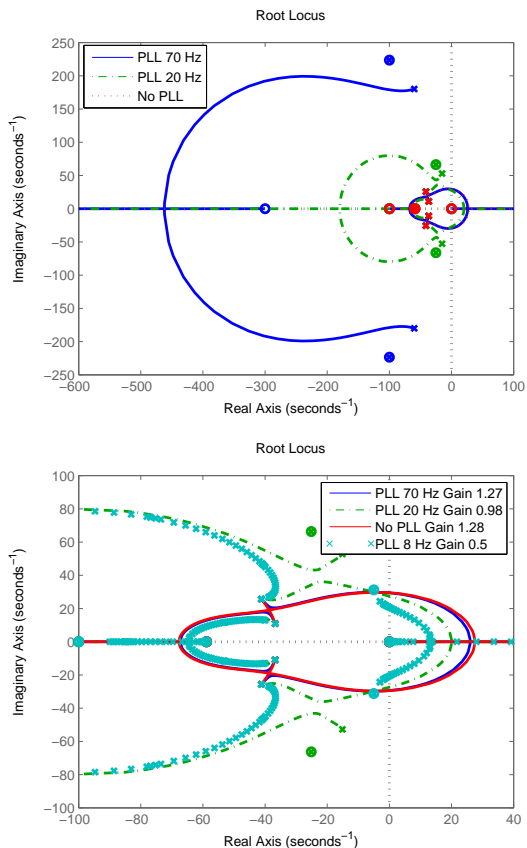


Fig. 21. Root loci based on  $G_{OL}$ . System parameters:  $X_g = 1$ ,  $P = 0.8$ .

Using the block diagram approach, we can clearly identify

the zeros and poles of each block and understand the mechanism of stability. Fig. 22 shows the root loci for the open-loop transfer function with PLL bandwidth at 20 Hz. As a comparison, the root loci related to PLL bandwidth at 8 Hz are also shown as dotted lines. We may see that for the two transfer functions with different PLL bandwidths, the poles related to Block 1 (power control and current tracking) and Block 3 (voltage control and current tracking) are the same. The pair of complex conjugate poles of Block 2 move towards the real axis and the imaginary axis when the PLL bandwidth changes from 20 Hz to 8 Hz. This indicates a reduced bandwidth for Block 2. In addition, the moving direction of this pair of poles changes from toward the LHP to towards the RHP.

Consider the case when PLL bandwidth is 20 Hz (solid line), Block 1 has a pair of complex conjugate poles  $-41.18 \pm j25.64$  and a zero  $-100$ . Block 2 has a pair of poles  $-15.0900 \pm j52.8232$ , and a zero  $-\frac{K_{iPLL} K_{pPLL}}{K_{pPLL}} = -100$ . Block 3 has poles  $-36.76 + j \pm 10.91$ , a zero at the origin point  $0 + j0$ , and another zero at  $-\frac{1}{\tau} = -58.82$ .

Two pair of the poles will be attracted to the three zeros ( $-100, -100, -58.82$ ) and  $-\infty$ . The rest pair of the poles will be attracted to the zero at the origin  $(0, 0)$  and  $+\infty$ . Therefore, as long as the open-loop system gain is overly large, the closed-loop system will prone to instability due a pair of complex conjugate open-loop poles moving to the RHP.

Fig. 22 clearly shows the effect of PLL dynamics on weak grid stability. A slower PLL makes the system more prone to instability.

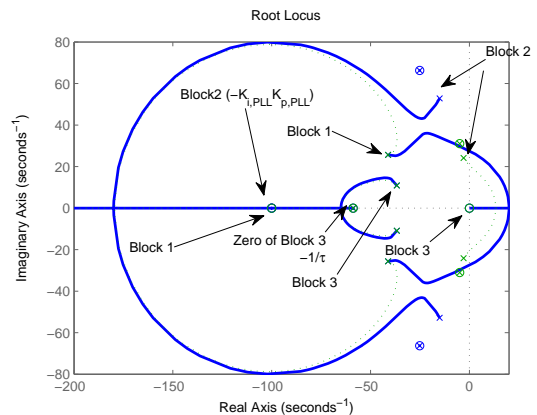


Fig. 22. Root loci based on  $G_{OL}$ . System parameters:  $X_g = 1$ ,  $P = 0.8$ . PLL bandwidth: 20 Hz (solid line), 8 Hz (dotted line).

*b) Effect of Power Level:* The block diagrams can clearly show the effect on open-loop poles and zeros due to power transfer increase. Note only Block 2's poles will be influenced by the power transfer level. The other two blocks have their poles and zeros intact with a varying power transfer level.

Consider the extreme case when the power transfer level is 1 pu and the SCR is 1 ( $X_g = 1$  pu). Given the grid voltage and the PCC voltage both at 1 pu, this power transfer level is at the steady-state limit. Block 2's poles for  $P = 0.99$  and  $P = 1.0$  are listed in Table V.

It can be seen that the two complex conjugate poles  $-3.55 \pm j26$  located in the LHP disappear, while two poles at  $(0, 0)$

TABLE V  
BLOCK 2'S POLES AND ZEROS

	$P = 0.99$	$P = 1.0$
Poles	$-25.15 \pm j66.31$	$-25.15 \pm j66.31$
Poles	$-3.55 \pm j26.4$	0, 0
Zeros	$-25.15 \pm j66.31$	$-25.15 \pm j66.31$
Zeros	-100	-100

appear when the power transfer reaches its steady-state limit. Indeed, when  $P = 1$  for  $X_g = 1$ , the  $q$ -axis current  $i_q = -1$ . The aforementioned statement is based on (8) ( $V_{PCC} = R_g i_d - X_g i_q + \sqrt{V_g^2 - (R_g i_q + X_g i_d)^2}$ ). Assuming that the grid resistance is 0, then the PCC voltage can be expressed as follows.

$$V_{PCC} = -X_g i_q + \sqrt{V_g^2 - (X_g i_d)^2}. \quad (21)$$

Note that  $P = V_{PCC} i_d$ , hence when  $P = 1$  and  $V_{PCC}$  is fixed at 1 pu,  $i_d$  is 1 pu. If the grid voltage  $V_g$  is assumed to be 1 pu, the second term of the right side of (21) is 0. Therefore, when  $X_g = 1$ ,  $i_q$  is indeed  $-1$ .

Examining the block diagram in Fig. 16, the entire Block 3 becomes  $(K_{pPLL} + \frac{K_{iPLL}}{s}) \frac{1}{s}$ . This is why two poles appear at the origin.

When the power transfer level has a slight increase toward the steady-state limit, the block related to PLL (Block 2) will see a pair of complex conjugate poles in LHP disappearing, while a pair of poles appearing at the origin point. This pair of poles cancels one zero at the origin introduced by Block 3, resulting in an unstable closed-loop system (shown in Fig. 23). Should the PLL dynamics be ignored, we will not be able to see any effect of this dramatic change on open-loop system poles and zeros due to power transfer change.

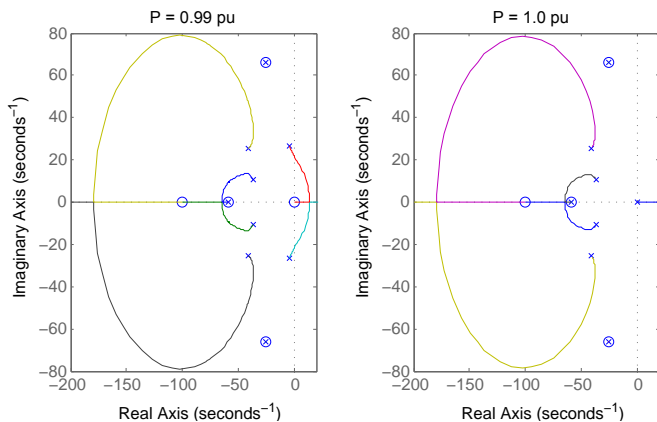


Fig. 23. Effect of power transfer level reaching steady-state limit on  $G_{OL}$  poles and zeros. PLL bandwidth: 20 Hz.

c) *Effect of Voltage Controller Parameters:* When the voltage controller's parameters increase, Block 3's poles' position will move to LHP and the gain of Block 3 will be reduced. The closed-loop system will have more stability margin. The root loci for two cases are shown in Fig. 24. It can be seen that increasing the gains of the voltage controller can improve the system stability. This observation corroborates the remarks in [2] and [3] that a faster voltage controller is better for stability.

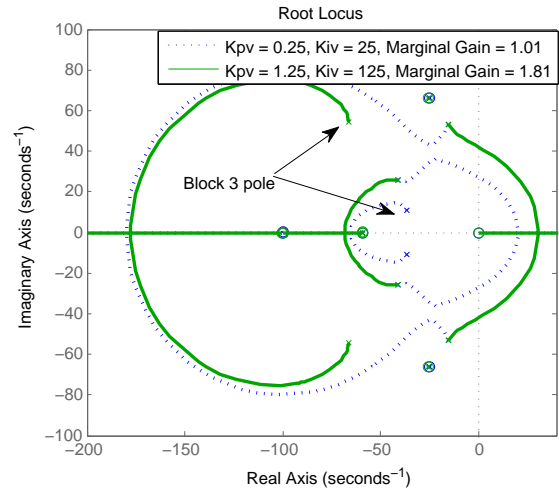


Fig. 24. Effect of voltage controller parameters on open-loop system poles and stability margin.

#### d) Remarks:

- It can be clearly seen that the power transfer level reflected by  $i_d$ , PCC voltage setting  $V_{PCC}$ , and grid reactance  $X_g$  influence the system stability through the open-loop transfer function's gain  $\frac{(X_g i_d)^2}{V_{PCC}}$ . High power transfer, low system strength and low PCC voltage setting make the open-loop transfer function gain larger and the closed-loop system more prone to oscillations and/or instability. The two factors, high power transfer and low SCR, have been mentioned in the literature, e.g., [5], [13]. Low voltage is another factor that induces oscillations. Thus, low voltage ride through [6] could also be an issue related to oscillations.
- The proportional and integral unit gains of the power controller, voltage controller, as well as the time constant of the current tracking change the position of poles and zeros, thus lead to effect on stability or instability. For example, the parameters of the voltage controller influence stability [2], [6], [13]. This effect is demonstrated in Fig. 24.
- Higher PLL bandwidth makes the system more stable. There are practical limitations posed for PLL gains and bandwidth. A few examples are given in the following to illustrate the limitations. Due to the noise and harmonics in measured signals, low-pass filters may be included in PLL [21]. For example, both ac and dc voltage filtering is employed to eliminate harmonics in PLL for a 2 MW Type-4 wind in [2]. The bandwidth of PLL will be limited by the low-pass filter. In addition, PLL design may consider compensators to deal with unbalance in voltage. For example, the design of PLL presented in Chapter 8 of [17] aims to provide filtering to the 120 Hz harmonics observed in the  $dq$  frame due to negative sequence voltage. The PLL's bandwidth thus is less than 120 Hz. In the example provided in Chapter 8 [17], the bandwidth of the PLL is about 30 Hz. This issue is particularly relevant for Type-4 wind where Low Voltage Ride Through (LVRT) is a requirement.

## VI. CONCLUSION

In this article, two simplified models for Type-4 wind with weak grid interconnection are examined and compared with a detailed model. Using the simplified model, mechanism of low-frequency oscillations is clearly explained. The root causes related to the critical mode are identified as weak grid, high wind power export, low voltage and low PLL bandwidth. The proposed model can accurately identify the critical mode related to the low-frequency oscillations and predict stability or instability.

## ACKNOWLEDGEMENT

The author would like to acknowledge the anonymous reviewers for their suggestions to improve this paper.

## REFERENCES

- [1] S.-H. Huang, J. Schmall, J. Conto, J. Adams, Y. Zhang, and C. Carter, "Voltage control challenges on weak grids with high penetration of wind generation: Ercot experience," in *Power and Energy Society General Meeting, 2012 IEEE*. IEEE, 2012, pp. 1–7.
- [2] N. P. Strachan and D. Jovcic, "Stability of a variable-speed permanent magnet wind generator with weak ac grids," *IEEE Transactions on Power Delivery*, vol. 25, no. 4, pp. 2779–2788, 2010.
- [3] Y. Zhou, D. Nguyen, P. Kjaer, and S. Saylor, "Connecting wind power plant with weak grid-challenges and solutions," in *Power and Energy Society General Meeting (PES), 2013 IEEE*. IEEE, 2013, pp. 1–7.
- [4] J. Hu, Y. Huang, D. Wang, H. Yuan, and X. Yuan, "Modeling of grid-connected dfig-based wind turbines for dc-link voltage stability analysis," *IEEE Transactions on Sustainable Energy*, vol. 6, no. 4, pp. 1325–1336, 2015.
- [5] J. Z. Zhou, H. Ding, S. Fan, Y. Zhang, and A. M. Gole, "Impact of short-circuit ratio and phase-locked-loop parameters on the small-signal behavior of a vsc-hvdc converter," *IEEE Transactions on Power Delivery*, vol. 29, no. 5, pp. 2287–2296, 2014.
- [6] J. Hu, Q. Hu, B. Wang, H. Tang, and Y. Chi, "Small signal instability of PLL-synchronized type-4 wind turbines connected to high-impedance AC grid during LVRT," *IEEE Transactions on Energy Conversion*, vol. 31, no. 4, pp. 1676–1687, 2016.
- [7] M. Zhao, X. Yuan, J. Hu, and Y. Yan, "Voltage dynamics of current control time-scale in a vsc-connected weak grid," *IEEE Transactions on Power Systems*, vol. 31, no. 4, pp. 2925–2937, 2016.
- [8] J. Hu, B. Wang, W. Wang, H. Tang, Y. Chi, and Q. Hu, "Small signal dynamics of dfig-based wind turbines during riding through symmetrical faults in weak ac grid," *IEEE Transactions on Energy Conversion*, vol. 32, no. 2, pp. 720–730, 2017.
- [9] H. Yuan, X. Yuan, and J. Hu, "Modeling of grid-connected VSCs for power system small-signal stability analysis in DC-link voltage control timescale," *IEEE Transactions on Power Systems*, vol. 32, no. 5, pp. 3981–3991, 2017.
- [10] Y. Huang and D. Wang, "Effect of control-loops interactions on power stability limits of vsc integrated to ac system," *IEEE Transactions on Power Delivery*, vol. 33, no. 1, pp. 301–310, 2018.
- [11] O. Goksu, R. Teodorescu, C. L. Bak, F. Iov, and P. C. Kjaer, "Instability of wind turbine converters during current injection to low voltage grid faults and pll frequency based stability solution," *IEEE Transactions on Power Systems*, vol. 29, no. 4, pp. 1683–1691, 2014.
- [12] D. Dong, B. Wen, D. Boroyevich, P. Mattavelli, and Y. Xue, "Analysis of phase-locked loop low-frequency stability in three-phase grid-connected power converters considering impedance interactions," *IEEE Transactions on Industrial Electronics*, vol. 62, no. 1, pp. 310–321, 2015.
- [13] L. Fan and Z. Miao, "An explanation of oscillations due to wind power plants weak grid interconnection," *IEEE Transactions on Sustainable Energy*, vol. 9, no. 1, pp. 488–490, 2018.
- [14] H. Ding, S. Fan, J. Z. Zhou, Y. Zhang, and A. M. Gole, "Parametric analysis of the stability of vsc-hvdc converters," in *11th IET International Conference on AC and DC Power Transmission*, Feb 2015, pp. 1–6.
- [15] Z. Yuan, Z. Du, C. Li, and T. An, "Dynamic equivalent model of vsc based on singular perturbation," *IET Generation, Transmission & Distribution*, vol. 10, no. 14, pp. 3413–3422, 2016.
- [16] L. Fan, *Control and Dynamics in Power Systems and Microgrids*. CRC Press, 2017.
- [17] A. Yazdani and R. Iravani, *Voltage-sourced converters in power systems: modeling, control, and applications*. John Wiley & Sons, 2010.
- [18] W. Leonhard, *Control of electrical drives*. Springer Science & Business Media, 2012.
- [19] T. Midtsund, J. Suul, and T. Undeland, "Evaluation of current controller performance and stability for voltage source converters connected to a weak grid," in *Power Electronics for Distributed Generation Systems (PEDG), 2010 2nd IEEE International Symposium on*. IEEE, 2010, pp. 382–388.
- [20] M. Amin, J. A. Suul, S. D'Arco, E. Tedeschi, and M. Molinas, "Impact of state-space modelling fidelity on the small-signal dynamics of vsc-hvdc systems," in *11th IET International Conference on AC and DC Power Transmission*, Feb 2015, pp. 1–11.
- [21] D. Jovcic, "Phase locked loop system for facts," *IEEE Transactions on Power Systems*, vol. 18, no. 3, pp. 1116–1124, 2003.
- [22] M. Cespedes and J. Sun, "Impedance modeling and analysis of grid-connected voltage-source converters," *IEEE Transactions on Power Electronics*, vol. 29, no. 3, pp. 1254–1261, 2014.



**Lingling Fan** is an Associate Professor with the University of South Florida, Tampa, where she has been since 2009. She was a Senior Engineer in the Transmission Asset Management Department, Midwest ISO, St. Paul, MN, from 2001 to 2007, and an Assistant Professor with North Dakota State University, Fargo, from 2007 to 2009. Her research interests include power systems and power electronics. Dr. Fan serves as an editor for IEEE Trans. Sustainable Energy.